

Chiral molecules on curved colloidal membranes.

Sk Ashif Akram¹, Arabinda Behera¹, Prerna Sharma² and Anirban Sain^{1,*}

¹ *Department of Physics, Indian Institute of Technology-Bombay, Powai, Mumbai 400076, India,* ² *Indian Institute of Science, Bangalore, 560012, India.*

(Dated: July 31, 2020)

Colloidal membranes, self assembled monolayers of aligned rod like molecules, offer a template for designing membranes with definite shapes and curvature, and possibly new functionalities in the future. Often the constituent rods, due to their molecular chirality, are tilted with respect to the membrane normal. Spatial patterns of this tilt on curved membranes result from a competition among depletion forces, nematic interaction, molecular chirality and boundary effects. We present a covariant theory for the tilt pattern on minimal surfaces, like helicoids and catenoids, which have been generated in the laboratory only recently. We predict several non-uniform tilt patterns, some of which are consistent with experimental observations and some, which are yet to be discovered.

PACS numbers:

INTRODUCTION

Rod like chiral molecules are used as a model system for studying how molecular chirality at microscopic scale generates self assembled structures at mesoscopic scales, often with multiple polymorphic forms [1]. Ability to switch between these forms require understanding of how these structures respond to physical factors like temperature, chemical environment, composition of the constituent rods and degree of their molecular chirality. In the presence of depletion agents, like nonadsorbing polymers, chiral or achiral rod like molecules (e.g., *fd* virus particles) can align and self assemble into monolayers that are one rod-length-thick and are often called colloidal membranes [2–4]. Unlike bilayer phospholipid membranes which typically form closed vesicles, colloidal membranes exhibit various open structures like flat circular discs, twisted ribbons [5], saddles and catenoids [6], in response to change of temperature, depletant concentration, or by mixing rods of different chirality, or rods of different lengths but same chirality.

Here we focus on colloidal membranes with curved surfaces. While flat circular discs are the most stable structures, a disc can be transformed into a twisted ribbon (helicoid) by lowering temperature [5] or by applying stretching force [7]. Lowering temperature is known to increase molecular chirality which in turn lowers the effective line tension at the membrane edges. This leads to proliferation of boundaries [5], and thus a switch from disc to a twisted ribbon. On the other hand mixing rods of two different lengths (but same chirality) generates membrane with negative gaussian curvatures as in saddles and catenoids [6]. This has been interpreted as the result of a positive gaussian curvature modulus (κ_G) [6, 8]. Interestingly, all these structures, namely, helicoid, catenoid are examples of minimal surfaces with zero mean curvature. That implies a large bending modulus (κ_B) for these membranes. Large bending energy cost not only favours generation of minimal surfaces, but it

also helps to minimize the tilt energy of the twisted chiral rods, which are otherwise frustrated on a flat membrane.

In Ref[7], it was shown that a disk shaped colloidal membrane can transform into a twisted ribbon under external stretching force. Here the contribution of the chiral nematic field, spread over the ribbon shaped membrane, was approximated to the energy of the open edges of the ribbon, assuming an uniform orientation of the rods in the bulk of the ribbon. It was argued that in the limit of small twist penetration depth (λ_p) all the twist is concentrated within a thin strip at the membrane edge. This could be a good approximation for disc shaped membranes [5, 9, 10] of typical radius $10\mu m$ and penetration depth $\sim 0.5\mu m$, which indeed shows chiral twist near the periphery and nearly uniform orientation of the rods in the bulk. However ribbons have typical half width of $\sim 1\mu m$ [5], comparable to λ_p , and also due to local membrane curvature the rods are not aligned across the width of the ribbon.

Here we take the reverse approach, i.e., assuming the membrane shape to be a minimal surface we seek the true lowest energy configuration of the chiral nematic field. We formulate a covariant theory for the chiral nematics on the curved surface and show, by minimizing the Frank free energy, that nontrivial nematic patterns can emerge on helicoid and catenoid shaped membranes.

The membrane surface, embedded in three dimensions, is described by the position vector $\vec{R} = [x(u, v), y(u, v), z(u, v)]$, where the two independent parameters (u, v) span the surface. The vectors defining the local tangent plane on the surface are $\vec{u} = \frac{\partial \vec{R}}{\partial u} = (x_u, y_u, z_u)$, and $\vec{v} = \frac{\partial \vec{R}}{\partial v} = (x_v, y_v, z_v)$ where subscripts denote partial derivatives, The metric g_{ij} on the this curved surface is obtained from the line element, $ds^2 = dx^2 + dy^2 + dz^2$. Expanding the differentials as

functions of the parameters u, v yields,

$$\begin{aligned} ds^2 &= (x_u du + x_v dv)^2 + (y_u du + y_v dv)^2 + (z_u du + z_v dv)^2 \\ &= (x_u^2 + y_u^2 + z_u^2) du^2 + (x_v^2 + y_v^2 + z_v^2) dv^2 \\ &\quad + 2(x_u x_v + y_u y_v + z_u z_v) du dv \\ &\equiv g_{ij} dx^i dx^j, \end{aligned}$$

Here g_{ij} ($i = 1, 2$) defines the 2×2 symmetric metric tensor on the surface, where $dx^1 = du$ and $dx^2 = dv$. The coefficients of du^2, dv^2 and $dudv$ (above) are identified as $g_{uu}, g_{vv}, 2g_{uv}$ ($= 2g_{vu}$), respectively. If \vec{u} and \vec{v} are orthogonal, and are along the principal axes, which is the case for all our applications, then g_{ij} is diagonal. It will be convenient to work with the normalised unit vectors $\hat{u} = \vec{u}/|\vec{u}|$, $\hat{v} = \vec{v}/|\vec{v}|$, and in our case $|\vec{u}| = \sqrt{g_{uu}}$ and $|\vec{v}| = \sqrt{g_{vv}}$. Although our nematic vector field $\hat{m}(u, v)$ is defined on the surface, both $\hat{m}(u, v)$ as well as its covariant tensorial derivatives (e.g., $\vec{\nabla} \times \hat{m}$) will have non-zero components perpendicular to the surface. Therefore we define unit normal to the surface $\hat{w} = \hat{u} \times \hat{v}$. The resulting local orthogonal frame $(\hat{u}, \hat{v}, \hat{w})$ can now be used for describing $\hat{m}(u, v)$ and its covariant derivatives. Since \hat{w} is the surface normal our curved surface can be defined as $w = w_0$ (constant) and therefore derivatives along the normal $\partial/\partial w$ yield zero. We will now generalise the line element ds^2 , mentioned above, for the 3D space by adding dw^2 to it. Thus g_{ij} is now enlarged to a 3×3 matrix with $g_{ww} = 1$, and the corresponding non-diagonal components $g_{uw} = g_{vw} = g_{wu} = g_{wv} = 0$.

Frank free energy on curved surface

Frank free energy of the nematic field $\hat{m}(u, v)$ on a curved surface can be written as

$$\begin{aligned} F &= \int \int \sqrt{g} du dv \frac{1}{2} \left[K_1 (\vec{\nabla} \cdot \hat{m})^2 + K_3 (\hat{m} \times \vec{\nabla} \times \hat{m})^2 \right. \\ &\quad + K_2 (\hat{m} \cdot \vec{\nabla} \times \hat{m} - q)^2 - K_{24} \hat{\nabla} \cdot [\hat{m} (\hat{\nabla} \cdot \hat{m}) + \hat{m} \times \vec{\nabla} \times \hat{m}] \\ &\quad \left. - C (\hat{m} \cdot \hat{w})^2 \right], \end{aligned} \quad (2)$$

where $\sqrt{g} du dv$ is the invariant area element (g being the determinant of g_{ij}). K_1, K_2 and K_3 are the splay, bend and twist modulus and henceforth we will work in the standard one constant approximation $K_1 = K_2 = K_3 = K$. Further, q is the intrinsic chirality of the nematic directors and C is the strength of the depletion interaction which promotes nematic alignment along the surface normal \hat{w} . Note that the chiral term which is linear in q will couple membrane curvature with nematic chirality [11, 12] via the use of covariant definition of curl. Since we work with finite surfaces with bounds $u \in [u_i, u_f]$ and $v \in [v_i, v_f]$, we also include the saddle-splay boundary term with modulus K_{24} . The term

$\hat{m} \times \vec{\nabla} \times \hat{m}$ can also be written as $-(\hat{m} \cdot \hat{\nabla}) \hat{m}$. Particularly, when the nematics prefers to orient normal to the surface (which is promoted by the depletion interaction here), the K_{24} has been shown to be important [13, 14]. Since all the moduli have the same dimension we will express them in units of K . Henceforth we use $K \equiv 1$ and $K_{24}/K \equiv K_{24}$.

The expressions for the covariant divergence and curl on curved surfaces are [15],

$$\begin{aligned} \text{Div}(\hat{m}) &= \vec{\nabla} \cdot \hat{m} = \frac{1}{\sqrt{g}} \partial_i \left(\sqrt{\frac{g}{g_{ii}}} m^i \right). \\ \text{Curl}(\hat{m}) &= \vec{\nabla} \times \hat{m} = \sqrt{\frac{g_{ii}}{g}} \epsilon^{ijk} \partial_j \left(\sqrt{g_{kk}} m^k \right) \hat{e}_i. \end{aligned} \quad (3)$$

Here $\{m^i\}$ are the components of the nematic vector expressed in terms of the normalised unit vectors $\hat{m} = m_u \hat{u} + m_v \hat{v} + m_w \hat{w}$. ϵ^{ijk} are the contravariant Levi-Civita-symbols, $\{\hat{e}_i\}$ are the unit vectors. In both the expressions above, sum is implied over repeated indices, however g_{ii} denote diagonal metric elements. The indices $(1, 2, 3)$ stand for the triad $(\hat{u}, \hat{v}, \hat{w})$.

Flat Disk

We first consider the simpler case of a circular, flat membrane as a disc of radius R . In cylindrical polar coordinates $(u, v, w) \equiv (r, \phi, z)$ and the surface is given by $\vec{R} = (r \cos \phi, r \sin \phi, 0)$, with $r < R$. The corresponding unit vectors $(\hat{u}, \hat{v}, \hat{w})$ are the standard polar $(\hat{r}, \hat{\phi}, \hat{z})$, and the diagonal metric tensor comes from the line element $ds^2 = dr^2 + r^2 d\phi^2 + dz^2$. While defining the orientation of the nematic director field all previous theoretical works [10, 16] had assumed the director $\hat{m}(r)$ to lie in the $(\hat{\phi}, \hat{z})$ plane making an inclination angle $\phi(r)$ with \hat{z} . In addition azimuthal symmetry (i.e., no dependence on ϕ) was also assumed. Here we relax the first assumption and allow \hat{m} to have a component along \hat{r} making an angle $\alpha(r)$ with the $(\hat{\phi}, \hat{z})$ plane. See Fig.2-a. Thus the director field is

$$\hat{m}[\phi(r), \alpha(r)] = (\sin \alpha, \cos \alpha \sin \phi, \cos \alpha \cos \phi). \quad (4)$$

Note that due to nematic symmetry i.e., invariance under inversion $\hat{m} \rightarrow -\hat{m}$, the orientation (ϕ, α) is same as $(\phi \pm \pi, -\alpha)$. Therefore, the allowed ranges for these angles can be $\phi \in [0, \pi]$ and $\alpha \in [-\pi/2, \pi/2]$. However in some plots later we allow the range $\phi \in [-\pi, \pi]$ so that the variation of nematic orientation appears continuous when ϕ goes across zero. Mapping the negative half of ϕ to the positive half by the shift $(\phi \rightarrow \phi + \pi, \alpha \rightarrow -\alpha)$ makes ϕ variation appear discontinuous and α suffers a slope discontinuity at the origin ($\phi = 0, \alpha = 0$), although spatially the variation is smooth. Using this parameterization for $\hat{m}(r)$ and the metric elements of the surface,

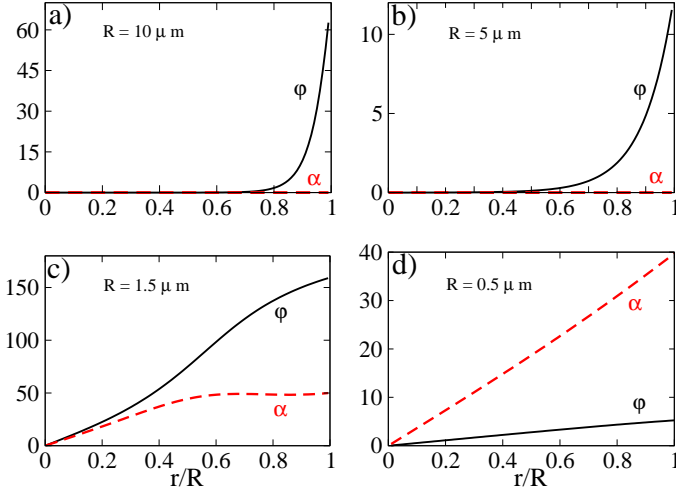


Figure 1: Inclination angles $\phi(r)$ and $\alpha(r)$ (in degrees) as functions of the scaled radial distance r/R from the center of the disk. (a-d) show solutions for different radii (see legends). Nonzero α is found only for small radii, much smaller than experimentally obtained disk radii $\sim 10\mu\text{m}$. System properties, the penetration depth $\lambda_p = 0.5\mu\text{m}$, $q = 0.5\mu\text{m}^{-1}$ and $K_{24} = 1$ are held fixed. Two typical nematic configurations, for $R = 10\mu\text{m}$ and $1.5\mu\text{m}$, are shown in fig.2.

Eq.3 yields

$$\begin{aligned}\vec{\nabla} \cdot \hat{m} &= \alpha'(r) \cos \alpha + \frac{\sin \alpha}{r} \\ \vec{\nabla} \times \hat{m} &= \left\{ \frac{\cos \alpha}{r} (r\phi' \cos \phi + \sin \phi) - \alpha' \sin \alpha \sin \phi, \right. \\ &\quad \left. \alpha' \sin \alpha \cos \phi + \phi' \cos \alpha \sin \phi, 0 \right\}\end{aligned}\quad (5)$$

The resulting Frank free-energy for this system is then,

$$\begin{aligned}F &= \int dr \frac{\pi}{r} \left\{ K_1 [r\alpha' \cos \alpha + \sin \alpha]^2 \right. \\ &\quad + K_2 [qr - \cos^2 \alpha (r\phi' + \sin \phi \cos \phi)]^2 \\ &\quad + \frac{K_3}{4} [r\{-4\alpha' \sin 2\alpha \sin^2 \phi + 4r\alpha'^2 \sin^2 \alpha + \sin^2 2\alpha\phi' \\ &\quad \times (r\phi' + \sin 2\phi)\} + \sin^2 \phi (4 \cos^4 \alpha \sin^2 \phi + \sin^2 2\alpha)] \\ &\quad - K_{24} r \left[\frac{1}{2} \alpha' \sin 2\alpha (\cos 2\phi - 5) - 2r\alpha'^2 \cos 2\alpha \right. \\ &\quad \left. - r\alpha'' \sin 2\alpha + \cos^2 \alpha \phi' \sin 2\phi - Cr^2 \cos^2 \alpha \cos^2 \phi \right\}\end{aligned}\quad (6)$$

Extremization of this free energy $F = \int dr \mathcal{F}$ (where \mathcal{F} is the free energy density) leads to two Euler-Lagrange equations which are $\frac{\partial}{\partial r} \left[\frac{\partial \mathcal{F}}{\partial \phi'(r)} \right] - \frac{\partial \mathcal{F}}{\partial \phi} = 0$ and $\frac{\partial}{\partial r} \left[\frac{\partial \mathcal{F}}{\partial \alpha'(r)} \right] - \frac{\partial \mathcal{F}}{\partial \alpha} = 0$. Nondimensionalised forms of these equations for the ϕ and α fields, respectively, are

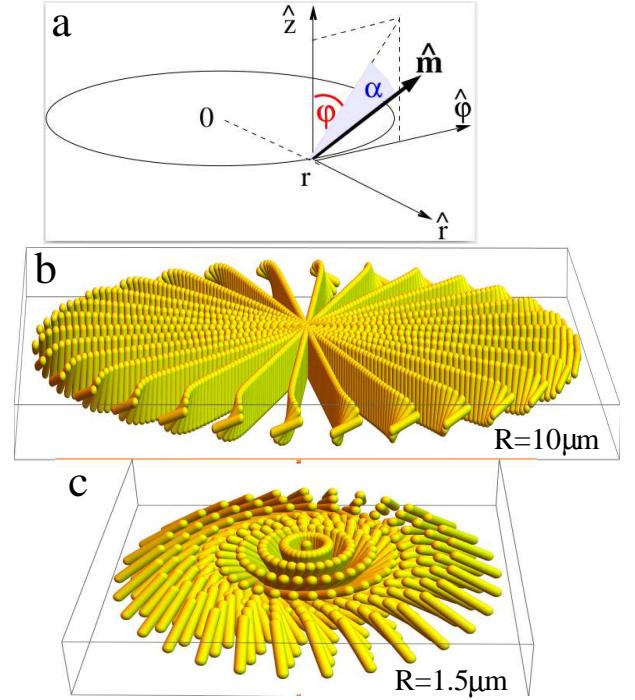


Figure 2: Nematic configurations for different disk radii at fixed $\lambda_p = 0.5\mu\text{m}$, $q = 0.5\mu\text{m}^{-1}$ and $K_{24} = 1$. a) defines the angles ϕ and α , (b-c) are for disk radii $R = 10$ and $1.5\mu\text{m}$. b) shows the deviation from vertical only at the periphery as seen in PolScope measurements [9]. c) shows exotic nematic orientation where the directors undergo large deviation from the normal. As we move radially outward, the director first turns parallel to the $x-y$ plane and then rises up, maintaining clockwise rotation all through, due to its chirality.

$$\begin{aligned}\frac{1}{r} \{ \cos^2 \alpha [\sin \phi \{ 2qr \sin \phi + (r^2 + 1) \cos \phi \} - r^2 \phi''(r) \\ + r\phi'(r)] \} - r\alpha'(r) (q - \phi'(r)) \sin 2\alpha = 0, \\ \text{and} \\ \frac{1}{4r} \{ 4qr^2 \sin 2\alpha \phi'(r) + 2qr \sin 2\alpha \sin 2\phi - 4r^2 \alpha''(r) \\ - 2r^2 \sin 2\alpha \phi'(r)^2 + r^2 \sin 2\alpha \cos 2\phi + r^2 \sin 2\alpha \\ - 4r\alpha'(r) + \sin 2\alpha \cos 2\phi + \sin 2\alpha \} = 0.\end{aligned}\quad (7)$$

Here the radius and the intrinsic chirality have been rescaled as $r' = r/\lambda_p$ and $q' = q\lambda_p$, by the twist penetration depth $\lambda_p = \sqrt{\frac{K}{C}}$ [10]. However, in what follows, we have omitted the primes to keep the notations simple. Note that the saddle-splay term, involving K_{24} , being a boundary term does not affect these equations but will show up in the boundary conditions (BC). The BC are as follows. The directors are assumed to be normal to the disc at its center i.e., $\phi(r=0) = \alpha(r=0) = 0$ and torque free BC [17] are imposed at the periphery, i.e., $\frac{\partial \mathcal{F}}{\partial \phi'(r)} = 0$ and $\frac{\partial \mathcal{F}}{\partial \alpha'(r)} = 0$, at $r = R$. In order to avoid numerical problems at $r = 0$, we use $r = r_0 = 10^{-6}$. The

torque free BC at the periphery amounts to

$$\cos^2 \alpha(R) \left[qR - \frac{K_{24} + 1}{2} \sin 2\phi(R) - R\phi'(R) \right] = 0, \quad (8)$$

$$\text{and, } \frac{\sin 2\alpha(R)}{4} \left[1 - 5K_{24} + (1 + K_{24}) \cos 2\phi(R) \right] + R\alpha'(R) \left[1 - 2K_{24} \cos 2\alpha(R) \right] = 0 \quad (9)$$

In the limit $\alpha = 0$ and $K_{24} = 0$, the first of these BCs' reduces to a form which is equivalent to $\hat{m} \cdot \vec{\nabla} \times \hat{m} - q = 0$, and the second one gives null.

We obtain numerical solution of this nonlinear, boundary value problem (Eq.7 along with Eq.8,9) using Mathematica. The angular orientation fields for flat circular discs have been measured experimentally using retardance [9]. It was found that the directors are nearly normal in the bulk of the disk and show large tilt, along the $\hat{\phi}$ direction, near the disk periphery. Our numerical solutions for the $R/\lambda_p \gg 1$ case shows the same exponential rise in inclination ϕ within the thin twist penetration layer, see Fig.1a,b and the corresponding director configuration in Fig.2b. The inclination $\alpha(r)$ however turns out to be zero for these disks, unless the disk radius is unrealistically small, as shown in Fig.1c,d. The corresponding director configuration is shown in Fig.2c, which is indeed exotic but probably is difficult to realise in experiments.

Helicoid

Now we discuss the director arrangement on a helicoidal membrane surface which is also known as a twisted ribbon. The parametric equation for the helicoidal surface, with pitch $2\pi C_1$, in the cartesian frame, is $\vec{R} = (u \cos v, u \sin v, C_1 v)$, where v is the angular coordinate and $u \in [-u_f, u_f]$ spans the width of the helicoid. The unit vectors \hat{u} and \hat{v} , constituting the tangent plane, and the surface normal $\hat{w} = \hat{u} \times \hat{v}$ are,

$$\left(\cos v, \sin v, 0 \right), \frac{1}{\sqrt{u^2 + C_1^2}} \left(-u \sin v, u \cos v, C_1 \right),$$

$$\text{and } \frac{1}{\sqrt{u^2 + C_1^2}} \left(C_1 \sin v, -C_1 \cos v, u \right). \quad (10)$$

The triad $(\hat{u}, \hat{v}, \hat{w})$ is shown in Fig.3a on the helicoid surface. From the line element on the surface $ds^2 = du^2 + (u^2 + C_1^2)dv^2 + dw^2$ we identify the components of the diagonal metric tensor. The director field in this $(\hat{u}, \hat{v}, \hat{w})$ frame using ϕ and α , defined as before in the disc case, is

$$\hat{m}[\phi(u), \alpha(u)] = (\sin \alpha, \cos \alpha \sin \phi, \cos \alpha \cos \phi). \quad (11)$$

Here, azimuthal symmetry i.e., dependence only on u , is assumed. As before, the projection of the director on (\hat{v}, \hat{w}) plane makes angle ϕ with \hat{w} (surface normal) and

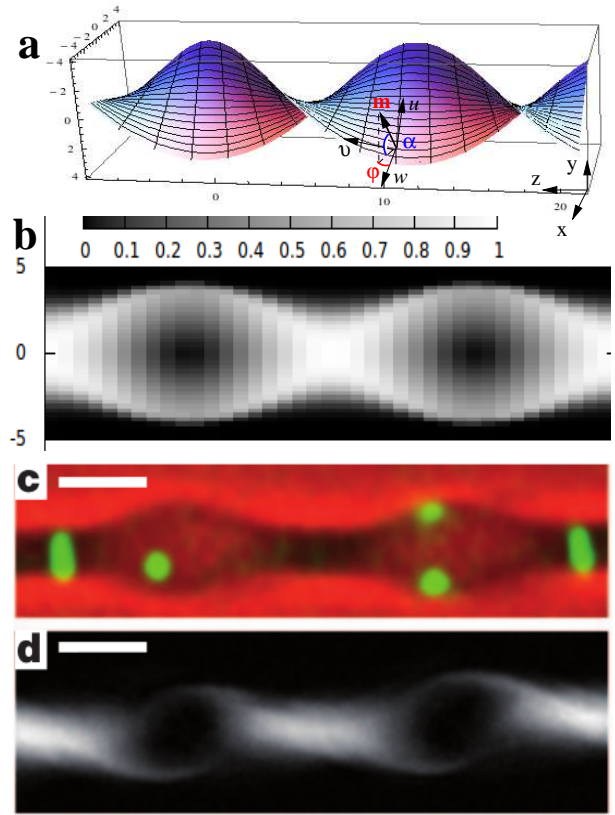


Figure 3: (a) shows local $(\hat{u}, \hat{v}, \hat{w})$ axes and the angles ϕ, α on the helicoidal surface. (b) is our theoretical plot corresponding to the ϕ profile in our Fig.4-a. (c,d) are experimental pictures from Ref[5] (with permission). (c) shows fluorescence (green) image of few rods, nearly parallel and perpendicular to the image plane at the helicoid neck and the bulge, respectively. (d) shows LC-PolScope image of the rods where the intensity at each pixel is proportional to $\sin^2 \theta$, where θ is the local tilt angle between the rod and the normal to the image plane (scale bars $2\mu m$). The small up-down asymmetry in (d) is because LC-PolScope image captures signal from one plane. Typically a stack of images are collected to infer the 3D structure (see for example, Fig.4e or f in Ref[5]). In (b), we show the same quantity, $\sin^2 \theta$ (color bar [0,1]), integrated over the 3D helicoid, corresponding to our solution in Fig.4-a, at fixed penetration depth $\lambda_p = 0.5\mu m$, $q = 0.5\mu m^{-1}$ and $K_{24} = 1$. Only small, gradual, deviation from normality occurs towards the edge of the helicoid. Here we treated $y - z$ plane as the image plane, with its normal along \hat{x} .

α is the inclination of the director to the (\hat{v}, \hat{w}) plane, see Fig.3-a. Thus the director has a component $\sin \alpha$ along \hat{u} . Using this parameterization for $\hat{m}(u)$ and the metric

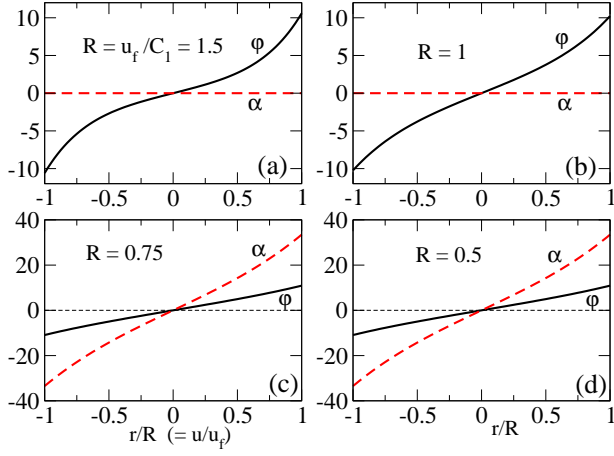


Figure 4: $\phi(r)$ and $\alpha(r)$ (in degrees) as functions of the scaled "radial" distance u/u_f (along the curved u axis), at fixed $\lambda_p = 0.5\mu\text{m}$, $q = 0.5\mu\text{m}^{-1}$ and $K_{24} = 1$. (a-d) show solutions for different helicoid widths u_f/C_1 (see legends), $2\pi C_1$ being the pitch. Nonzero α is predicted only for narrow helicoids (c and d) with small u_f/C_1 . Experimentally obtained ones [5] have $u_f/C_1 \sim 1$. Two representative nematic arrangements on helicoids are shown in Fig.5.

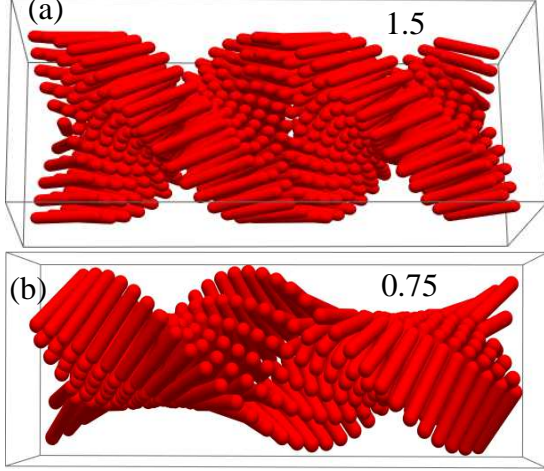


Figure 5: (a,b) Shows nematic arrangements on helicoidal surfaces, corresponding to Fig.4-a and -c. The scaled helicoidal widths u_f/C_1 are mentioned in the legends. In (b) deviation from the (v, w) plane (i.e., nonzero α) is manifest.

elements of the surface, Eq.3 yields

$$\begin{aligned}\vec{\nabla} \cdot \vec{m} &= \frac{\partial_u(\sqrt{u^2 + C_1^2} m_u)}{\sqrt{u^2 + C_1^2}} + \frac{\partial_v m_v}{\sqrt{u^2 + C_1^2}} + \partial_w m_w \\ \vec{\nabla} \times \vec{m} &= \left(\frac{1}{\sqrt{u^2 + C_1^2}} \partial_v m_w - \partial_w m_v, \partial_w m_u - \partial_u m_w, \right. \\ &\quad \left. \frac{1}{\sqrt{u^2 + C_1^2}} (\partial_u(\sqrt{u^2 + C_1^2} m_v) - \partial_v m_u) \right) \quad (12)\end{aligned}$$

Here $\vec{m} = m_u \hat{u} + m_v \hat{v} + m_w \hat{w}$ and $\partial_w \vec{m} = 0$.

Following the same recipe as before, i.e., defining $\lambda_p =$

$\sqrt{\frac{K}{C}}$, using dimensionless variables $r \equiv u/C_1$, $q \equiv q\lambda_p$, and $C_1 \equiv C_1/\lambda_p$ the Frank free energy density is

$$\begin{aligned}\mathcal{F} &= \frac{1}{2(r^2 + 1)^{3/2}} \left\{ K_1 [(r^2 + 1) \alpha' \cos \alpha + r \sin \alpha]^2 \right. \\ &+ K_2 [C_1 q (r^2 + 1) - \cos^2 \alpha ((r^2 + 1) \phi' + r \sin \phi \cos \phi)]^2 \\ &+ K_3 [(r^2 + 1)((r^2 + 1) \alpha' (r)^2 \sin^2 \alpha + \sin^2 \alpha \cos^2 \alpha \phi' \\ &\quad \times ((r^2 + 1) \phi' + r \sin 2\phi) - r \alpha' \sin 2\alpha \sin^2 \phi) \\ &\quad \left. + r^2 \cos^4 \alpha \sin^2 \phi (\tan^2 \alpha + \sin^2 \phi)] \right. \\ &- K_{24} [(\sin^2 \alpha - \cos^2 \alpha \sin^2 \phi) + \frac{(1 + r^2)}{2} \\ &\quad \times \{ r(5 - \cos 2\phi) \sin 2\alpha \alpha' + 4(1 + r^2) \cos 2\alpha \alpha'^2 \\ &\quad \left. - 2r \cos^2 \alpha \sin 2\phi \phi' + 2(1 + r^2) \sin 2\alpha \alpha'' \}] \\ &\left. - C C_1^2 (r^2 + 1)^2 \cos^2 \alpha \cos^2 \phi \right\}. \quad (13)\end{aligned}$$

This free energy density is expected to be symmetric with respect to $r \rightarrow -r$, i.e., the two strips of the helicoid at positive and negative r should have the same free energy density. Mathematically, this can be realised if ϕ, α are odd functions of r , and consequently ϕ', α' are even functions. Later we show that free energy minimization indeed leads to such solutions for both helicoids and catenoids (to be discussed later). Using one constant approximation, the Euler-Lagrange's equations yield,

$$\begin{aligned}\frac{1}{(r^2 + 1)^{3/2}} \{ \cos \alpha \{ \cos \alpha (\sin \phi ((C_1^2 (r^2 + 1)^2 + r^2 - 1) \cos \phi \\ + 2C_1 q r (r^2 + 1) \sin \phi) - r(r^2 + 1) \phi'(r) - (r^2 + 1)^2 \phi''(r)) \\ - 2(r^2 + 1)^2 \alpha'(r) \sin \alpha (C_1 q - \phi'(r)) \} \} = 0. \quad (14)\end{aligned}$$

and,

$$\begin{aligned}\frac{1}{\sqrt{r^2 + 1}} \{ \sin 2\alpha ((C_1^2 (r^2 + 1)^2 + r^2 - 1) \cos^2 \phi + \\ C_1 q r (r^2 + 1) \sin 2\phi + (r^2 + 1)^2 \phi'(r) (2C_1 q - \phi'(r))) - \\ 2(r^2 + 1) ((r^2 + 1) \alpha''(r) + r \alpha'(r)) \} = 0. \quad (15)\end{aligned}$$

The BC are similar as before, i.e., at the central line of the helicoid $\alpha(r = 0) = \phi(r = 0) = 0$. As before, the open edges of the helicoid, at $r = \pm R = \pm u_f/C_1$, are considered to be torque free, which yields,

$$\cos^2 \alpha \left[\phi' - C_1 q + (K_{24} + 1) \frac{R \sin 2\phi}{2(R^2 + 1)} \right] = 0,$$

and,

$$\begin{aligned}\frac{R \sin 2\alpha}{4(R^2 + 1)} \left[1 - 5K_{24} + (1 + K_{24}) \cos 2\phi \right] \\ + \alpha' [1 - 2K_{24} \cos 2\alpha] = 0. \quad (16)\end{aligned}$$

Due to spatially varying principle curvatures (although the mean curvature is zero), the solutions for helicoids, obtained here, are more complex. Qualitatively two different type of solutions emerge : 1) with $\alpha = 0$ (shown in Fig.4-a,b), and 2) $\alpha \neq 0$ (shown in Fig.4-c,d), while ϕ remains small for both cases. Two representative nematic

configurations, corresponding to Fig.4-a and c are shown in Fig.5. Experimentally obtained helicoids (twisted ribbons) [5] have pitch $\sim 6\mu\text{m} = (2\pi C_1)$ and width $\sim 2\mu\text{m} = (2u_f)$, which yields $u_f/C_1 \sim 1$. We therefore pick Fig.4-b for computing pixel intensities $I \propto \sin^2 \theta$, as detected by LC-PolScope images, where θ is the angle between the nematic director and the normal (\hat{x}) to the image plane ($y-z$) here. For example, the part of the ribbon where the directors point along \hat{x} should appear dark. The computed intensity map is shown in Fig.3-b and compared with experimental image [5] in Fig.3-d. The intensity is obtained by computing $\cos \theta = \hat{m} \cdot \hat{x}$, where \hat{x} pertains to the cartesian lab frame. Using Eq.10 and 11 we get,

$$\cos \theta = \sin \alpha \cos v + \frac{\cos \alpha \sin v}{\sqrt{1 + (u/C_1)^2}} \left\{ \cos \phi - \frac{u}{C_1} \sin \phi \right\},$$

which for $\alpha = 0$ yields,

$$\sin^2 \theta = 1 - \frac{\sin^2 v}{1 + (u/C_1)^2} \left(\cos \phi - \frac{u}{C_1} \sin \phi \right)^2. \quad (17)$$

Note that since ϕ and α are odd functions of u , under the change $u \rightarrow -u$ the intensity remains same. It implies that the strips belonging to positive and negative u parts of the ribbon must produce the same intensity. This is manifest in the theoretical map Fig.3-b. However, in the experimental image (Fig.3-d) the asymmetry (as explained in the caption) occurs due to the fact that a LC-PolScope image captures signal from a particular plane. Typically, by varying this plane a stack of images (z -stack) are collected to infer the 3D structure (such a stack is shown in Fig.4e and f in Ref-[5]).

CATENOID

Now we consider the chiral nematic field on a catenoid shaped membrane surface. Taking advantage of the azimuthal symmetry of the catenoid, the director field at different x-y planes can be measured using confocal microscopy and preliminary results indicate nontrivial patterns [6] with nonzero α in the bulk and $\alpha \rightarrow 0$ at the free edges.

The parametric equation for such a surface in cartesian frame is given by

$$\vec{R} = \left(C_1 \cosh \left[\frac{v}{C_1} \right] \cos u, C_1 \cosh \left[\frac{v}{C_1} \right] \sin u, v \right), \quad (18)$$

where $u \in [0, 2\pi]$ is the angular coordinate and $v \in [-v_f, v_f]$ is the distance along the longitudinal direction of the catenoid. C_1 is the cross sectional radius of the catenoid at $v = 0$. The resulting triad $(\hat{u}, \hat{v}, \hat{w})$, shown in Fig.6, are

$$\left(-\sin u, \cos u, 0 \right), \left(\tanh \left[\frac{v}{C_1} \right] \cos u, \tanh \left[\frac{v}{C_1} \right] \sin u, \text{sech} \left[\frac{v}{C_1} \right] \right) \text{ and } \left(\text{sech} \left[\frac{v}{C_1} \right] \cos u, \text{sech} \left[\frac{v}{C_1} \right] \sin u, -\tanh \left(\frac{v}{C_1} \right) \right)$$

The projection of the director on (\hat{u}, \hat{w}) plane makes angle ϕ with \hat{w} (surface normal) and α is the inclination

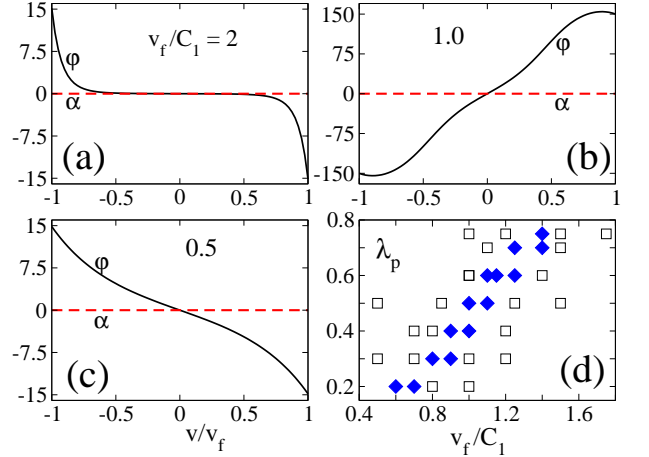
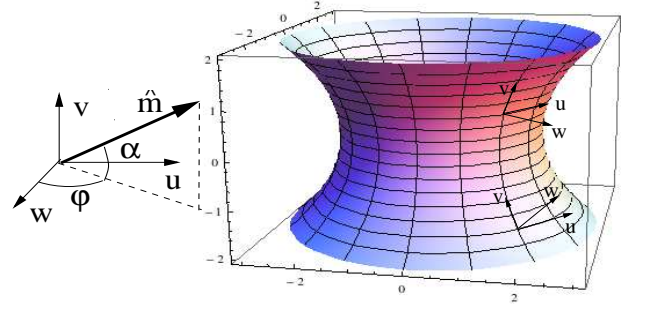


Figure 7: $\phi(r)$ and $\alpha(r)$ (in degrees) as functions of the scaled distance v/v_f (along curved surface). Here we have fixed $\lambda_p = 0.5\mu\text{m}$, $q = 0.5\mu\text{m}^{-1}$ and $K_{24} = 1$, and applied two torque free BCs (see text). (a-c) show solutions for catenoids of different aspect ratios v_f/C_1 (see legends), C_1 being the minimum neck radius. Experimentally observed ones [6] have $v_f/C_1 \sim 1.3$. With the two torque free BCs (see text) we do not get $\alpha \neq 0$ solutions, contrary to experimental findings [6]. Two representative nematic arrangements are shown in Fig.8. (d) shows a phase diagram with respect to two parameters λ_p and v_f/C_1 . Two type of solutions emerge, small ϕ , as in 'a' or 'c' (open squares), and large ϕ , as in 'b' (solid diamonds).

Using line element,

$$ds^2 = \cosh^2 \left(\frac{v}{C_1} \right) dv^2 + C_1^2 \cosh^2 \left(\frac{v}{C_1} \right) du^2 + dw^2 \quad (19)$$

we construct the metric. Further, the director field is defined using two angles ϕ and α (see Fig.6), in this $(\hat{u}, \hat{v}, \hat{w})$ frame, as

$$\hat{m}[\phi(v), \alpha(v)] = (\cos \alpha \sin \phi, \sin \alpha, \cos \alpha \cos \phi). \quad (20)$$

Here, azimuthal symmetry i.e., no dependence on u , is assumed. Further, the director does not lie fully in the (\hat{u}, \hat{w}) plane, but may have a nonzero component along \hat{v} . The projection of the director on (\hat{u}, \hat{w}) plane makes angle ϕ with \hat{w} (surface normal) and α is the inclination

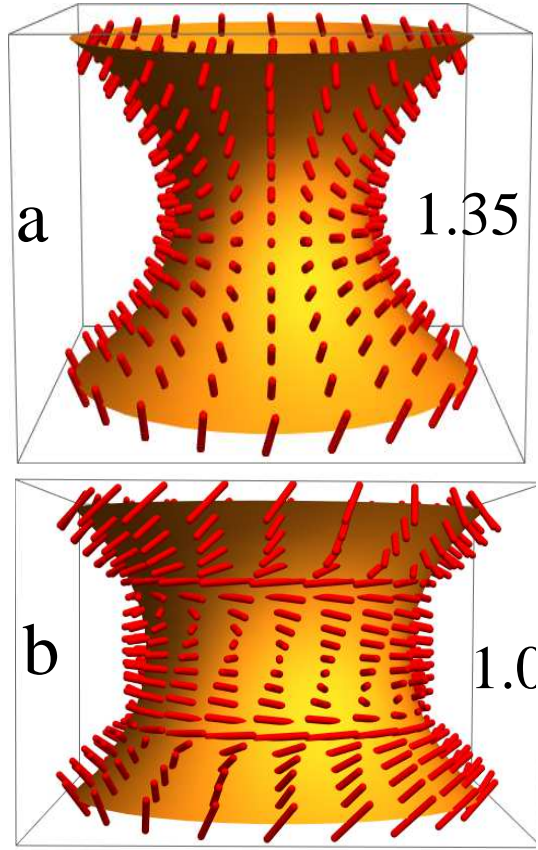


Figure 8: (a) and (b) show nematic arrangements (on catenoid surfaces (yellow)), corresponding to the same large ϕ solutions, respectively, in Fig.7. The aspect ratios v_f/C_1 are shown in the legends. In (b) the director field is clockwise, as we move upwards along increasing v .

of the director with the (\hat{u}, \hat{w}) plane. Thus the director has a component $\sin \alpha$ along \hat{v} . Using $\hat{m}(v)$ and the metric elements of the surface, Eq.3 yields, after rescaling $v/C_1 \rightarrow v$,

$$\begin{aligned} \vec{\nabla} \cdot \vec{m} &= \frac{\text{sech}(v)}{C_1} [\alpha'(v) \cos \alpha + \tanh(v) \sin \alpha], \text{ and} \\ \vec{\nabla} \times \vec{m} &= \left\{ \frac{\text{sech}(v)}{C_1} \{ \alpha'(v) \sin \alpha \sin \phi - \cos \alpha [\phi'(v) \cos \phi \right. \\ &\quad \left. + \tanh(v) \sin \phi] \}, -\frac{\text{sech}(v)}{C_1} \{ \alpha'(v) \sin \alpha \cos \phi \right. \\ &\quad \left. + \cos \alpha \phi'(v) \sin \phi \}, 0 \right\} \end{aligned} \quad (21)$$

Here $\vec{m} = m_u \hat{u} + m_v \hat{v} + m_w \hat{w}$ and $\partial_w \vec{m} = 0$. Defining $\lambda_p = \sqrt{\frac{K}{C}}$ (where $K_1 = K_2 = K_3 = K$) and using dimensionless variables $v \equiv v/C_1$, $q \equiv q\lambda_p$ and $C_1 \equiv$

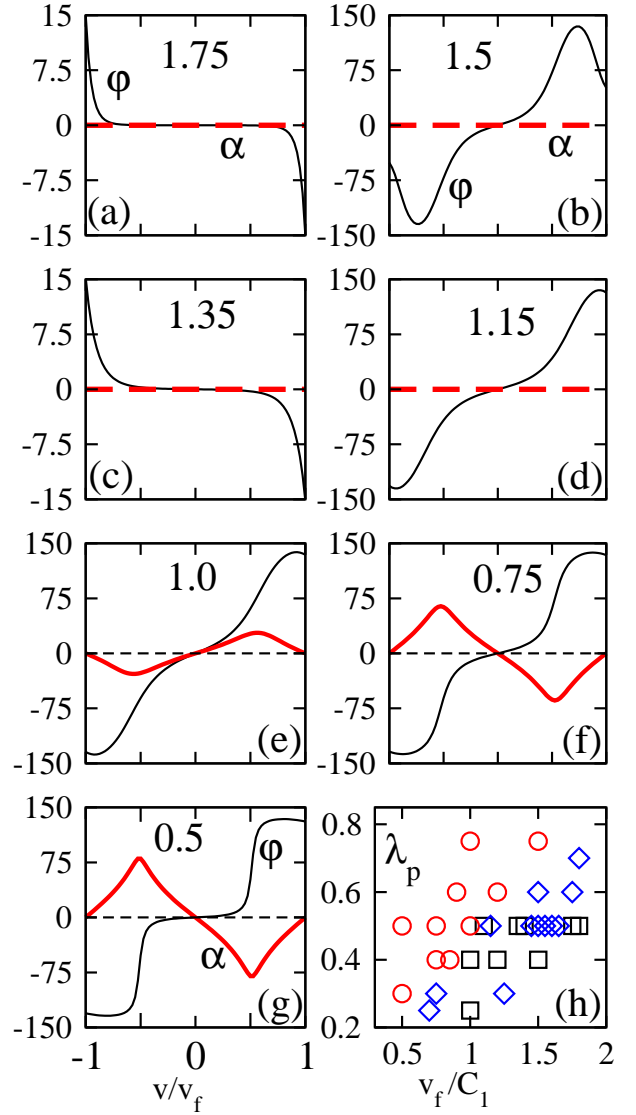


Figure 9: $\phi(r)$ and $\alpha(r)$ (in degrees) as functions of the scaled distance v/v_f . We fixed $\lambda_p = 0.5\mu m$, $q = 0.5\mu m^{-1}$ and $K_{24} = 1$, and employed torque free BC with respect to ϕ , and set $\alpha(\pm v_f) = 0$ at the open boundaries (edges). (a-g) are for different aspect ratios v_f/C_1 (see legends). Two representative nematic arrangements are shown in Fig.10. (h) shows a phase diagram based on the two types of solutions that emerge in (a-g): 1) $\alpha \neq 0$ (red circles) at $v_f/C_1 \leq 1$, and 2) $\alpha = 0$ at larger $v_f/C_1 \geq 1$. However, the $\alpha = 0$ type has two sub-types, small ϕ (black squares) and large ϕ (blue diamonds), with no sharp boundary between them.

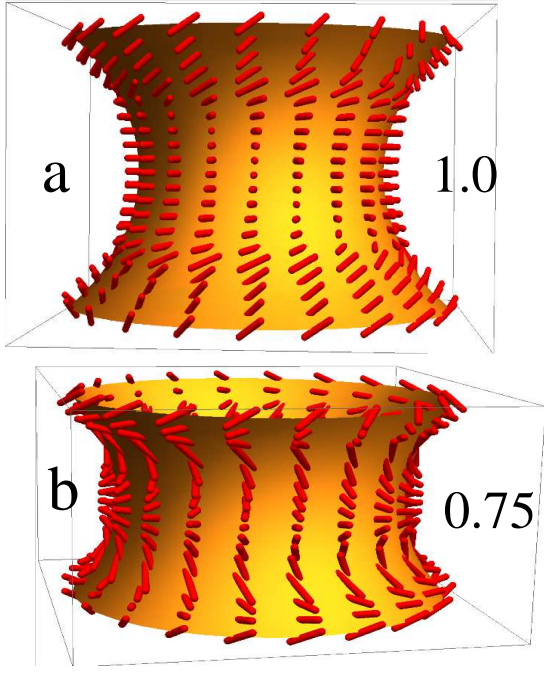


Figure 10: (a) and (b) show nematic arrangements (red) on catenoid surfaces (yellow), corresponding to $\alpha(r) \neq 0$ cases in Fig.9-e and f, respectively. The aspect ratios v_f/C_1 are shown in the legends. Unidirectional rotation of the director along increasing v is visible.

C_1/λ_p , the Frank Free energy reads,

$$\begin{aligned}
\mathcal{F} = & \frac{1}{2} \left\{ K_1 [\alpha' \cos \alpha + \tanh v \sin \alpha]^2 \right. \\
& + K_2 (C_1 q \cosh v + \cos^2 \alpha [\phi' + \tanh v \sin \phi \cos \phi])^2 \\
& + K_3 (-\alpha' \tanh v \sin 2\alpha \sin^2 \phi + \alpha'^2 \sin^2 \alpha \\
& \quad + \cos^2 \alpha (\phi' \sin^2 \alpha [\phi' + \tanh v \sin 2\phi] \\
& \quad + \tanh^2 v \sin^2 \phi (\cos^2 \alpha \sin^2 \phi + \sin^2 \alpha)) \\
& - \frac{K_{24}}{C_1} \left[\text{sech } v (\text{sech}^2 v \sin^2 \alpha + C_1 \cos^2 \alpha \text{sech } v \sin^2 \phi \right. \\
& \quad - \sin^2 \alpha \tanh^2 v) + \alpha' \tanh v \sin 2\alpha \left(\frac{\text{sech } v}{2} - C_1 \sin^2 \phi \right) \\
& \quad + \alpha'^2 \cos 2\alpha (-C_1 + \text{sech } v) + C_1 \phi' \cos^2 \alpha \sin 2\phi \tanh v \\
& \quad \left. + \alpha'' \cos \alpha \sin \alpha (-C_1 + \text{sech } v) \right] \\
& \left. - CC_1^2 \cosh^2 v \cos^2 \alpha \cos^2 \phi \right\} \quad (22)
\end{aligned}$$

Here we retained the different K_j 's to keep track of the splay, twist and bend contributions. As mentioned before, the free energy density has the $v \rightarrow -v$ symmetry provided ϕ, α are odd functions of v . The corresponding Euler-Lagrange equations are,

$$\begin{aligned}
& \frac{1}{2} \cos^2 \alpha [C_1^2 \cosh^2(v) \sin 2\phi - 4C_1 q \sinh(v) \sin^2 \phi \\
& - 2\phi''(v) + \tanh^2(v) \sin 2\phi - \text{sech}^2(v) \sin 2\phi] \\
& + \alpha'(v) \sin 2\alpha [C_1 q \cosh(v) + \phi'(v)] = 0. \quad (23)
\end{aligned}$$

and,

$$\begin{aligned}
& \frac{1}{4} (\sin 2\alpha (2C_1^2 \cosh^2(v) \cos^2 \phi - 2C_1 q \sinh(v) \sin 2\phi \\
& - 2\text{sech}^2(v) \cos^2 \phi + \tanh^2(v) \cos 2\phi + \tanh^2(v)) \\
& - 4C_1 q \cosh(v) \sin 2\alpha \phi'(v) - 4\alpha''(v) - 2 \sin 2\alpha \phi'(v)^2) = 0. \quad (24)
\end{aligned}$$

We impose similar boundary conditions as before: 1) at the center of the catenoid, at $v = 0$, $\alpha(0) = \phi(0) = 0$, consistent with ϕ, α being odd functions, and 2) the upper and lower edges of the catenoid ($v = \pm v_f$) are torque free, imposing $\frac{\partial \mathcal{F}}{\partial \phi'(r)} = 0$ and $\frac{\partial \mathcal{F}}{\partial \alpha'(r)} = 0$. That yields

$$\begin{aligned}
& \cos^2 \alpha [2C_1 q \cosh v_f + (1 - K_{24}) \tanh v_f \sin 2\phi + 2\phi'] = 0 \quad (25) \\
& \text{and, } 4\alpha' [K_{24}(C_1 - \text{sech } v_f) \cos 2\alpha + C_1] + \tanh v_f \sin 2\alpha \\
& \quad \times [2C_1 - K_{24} \text{sech } v_f + 2C_1(K_{24} - 1) \sin^2 \phi] = 0 \quad (26)
\end{aligned}$$

With these boundary conditions the Euler equation fail to produce any $\alpha \neq 0$ solution, for catenoids with experimentally observed [6] aspect ratios $v_f/C_1 \sim 1.3$ (with $v_f \sim 2.8 \mu\text{m}$ and $C_1 \sim 2.1 \mu\text{m}$). In Fig7a-c we show the variation of ϕ, α with v , at different aspect ratios v_f/C_1 . There are two types of solutions, which exhibit small (up to 15°) and large (up to 150°) values of ϕ . Fig7-d shows a phase diagram where large ϕ solutions are confined in a narrow strip bordered by small ϕ solutions. In Fig8 we show the nematic arrangements corresponding to, a) small ϕ , and b) large ϕ solutions. In 'b' the director is normal to the surface at $v = 0$. As $|v|$ increases it gradually turns parallel to the surface and later again turns away from the surface towards surface normal. Due to fixed intrinsic chirality the director maintains an uniform direction of rotation (clockwise here) towards increasing v .

Analysis of the boundary conditions Eqs.25,26 reveals that in order to realise $\alpha = 0$ at the edges (as measured in experiments) α' also has to be zero there. Numerical solutions in Fig7a-c (using Mathematica) does not admit such solutions. We therefore explore another boundary condition where α will be set to zero at the edges, dropping the torque free BC (Eq.26) with respect to α . The other torque free BC with respect to ϕ (Eq.25) is retained. The only justification for this $\alpha(\pm v_f) = 0$ BC is phenomenology, as we are not aware of any other physical reasoning. Similar BC has been applied before at the boundary of 3D structures [15].

With this BC, solutions with nonzero α arise for catenoids with small aspect ratios $v_f/C_1 \leq 1$. Fig9a-g show solutions for $\phi(v), \alpha(v)$ for different aspect ratios. Three different type of solutions arise (described in the caption of Fig.9). Subplot (h) shows a phase diagram populated by these solutions. Broadly, $\alpha \neq 0$ solutions appear for large λ_p and helicoids with small aspect ratios. In these solutions $|\phi|$ keep increasing towards the edges

upto $\sim 140^\circ$. This feature qualitatively matches with experiments, however in experiments ϕ reaches upto 90° . At small aspect ratios (Fig9f,g), ϕ shows abrupt jumps along the non-azimuthal direction v , which is reminiscent of domain boundaries. In Fig.10 two representative nematic arrangements corresponding to $\alpha \neq 0$ solutions are shown.

For all the ϕ, α plots (for disk, helicoid and catenoid) we used representative values $q = 0.5\mu m^{-1}$, $\lambda_p = 0.5\mu m$, $K_{24}/K = 1$. Changing these values merely shift the the phase boundaries but do not change the qualitative nature of the solutions. Further, since we used nondimensional variable $q\lambda_p$, change of λ_p at fixed q will have the same effect as changing q keeping λ_p fixed.

In summary, we examined how rod like molecules preferentially arrange on a curved colloidal membranes having the shape of minimal surfaces. In particular, we focused on possible departure of the rods (by angle α) from the plane formed by the surface normal and the azimuthal tangent vector. This was motivated by recent measurements on catenoid shaped colloidal membranes [6]. We also showed how changing boundary conditions change the nature of the solutions and allow comparison of theory to experimental measurements. It was interesting that for disks and helicoids, torque free BC with respect to both ϕ and α reproduce experimental results, however for catenoids a more phenomenological BC $\alpha(\pm v_f) = 0$ had to be adopted to produce nonzero α . Our phase diagrams summarise how the nature of the solutions depend on material property (λ_p) and the geometry of the surface (via aspect ratio). However, we note that a complete solution to this problem will require simultaneous minimization of the membrane geometry and the director configuration, which requires optimization in a bigger parameter space. Although colloidal membranes with minimal surfaces have been realised in the laboratory, measuring precise director orientations remain challenging. Our theoretical predictions will motivate this effort.

ACKNOWLEDGEMENTS

AA and AS acknowledge Science and Engineering Research Board (SERB), India (Project No. CRG/2019/005944), and IRCC-IIT Bombay, India for financial support. AB thanks UGC-India for financial

support. PS acknowledges SERB, India (Project No. CRG/2019/000855) for funding.

* asain@phy.iitb.ac.in

-
- [1] A. Aggeli, I. A. Nyrkova, M. Bell, R. Harding, L. Carrick, T. C. McLeish, A. N. Semenov, and N. Boden, Proceedings of the National Academy of Sciences **98**, 11857 (2001).
 - [2] E. Barry, D. Beller, and Z. Dogic, Soft Matter **5**, 2563 (2009).
 - [3] E. Barry and Z. Dogic, Proceedings of the National Academy of Sciences **107**, 10348 (2010).
 - [4] L. Saikia, T. Sarkar, M. Thomas, V. Raghunathan, A. Sain, and P. Sharma, Nature communications **8**, 1160 (2017).
 - [5] T. Gibaud, E. Barry, M. J. Zakhary, M. Henglin, A. Ward, Y. Yang, C. Berciu, R. Oldenbourg, M. F. Hagan, D. Nicastro, et al., Nature **481**, 348 (2012).
 - [6] A. Balchunas, P. Sharma, and Z. Dogic, in *APS March Meeting Abstracts* (2017), vol. 2017 of *APS Meeting Abstracts*, p. C17.011.
 - [7] A. Balchunas, L. L. Jia, M. J. Zakhary, J. Robaszkowski, T. Gibaud, Z. Dogic, R. A. Pelcovits, and T. R. Powers, Physical Review Letters **125**, 018002 (2020).
 - [8] T. Gibaud, C. N. Kaplan, P. Sharma, M. J. Zakhary, A. Ward, R. Oldenbourg, R. B. Meyer, R. D. Kamien, T. R. Powers, and Z. Dogic, Proceedings of the National Academy of Sciences **114**, E3376 (2017).
 - [9] E. Barry, Z. Dogic, R. B. Meyer, R. A. Pelcovits, and R. Oldenbourg, The Journal of Physical Chemistry B **113**, 3910 (2009).
 - [10] R. A. Pelcovits and R. B. Meyer, Liquid Crystals **36**, 1157 (2009).
 - [11] J. V. Selinger and J. M. Schnur, Physical review letters **71**, 4091 (1993).
 - [12] W. Helfrich and J. Prost, Physical Review A **38**, 3065 (1988).
 - [13] V. H. Schmidt, Physical review letters **64**, 535 (1990).
 - [14] D. W. Allender, G. Crawford, and J. Doane, Physical review letters **67**, 1442 (1991).
 - [15] J. P. McInerney, P. W. Ellis, D. Z. Rocklin, A. Fernandez-Nieves, and E. A. Matsumoto, Soft matter **15**, 1210 (2019).
 - [16] L. Kang and T. C. Lubensky, Proceedings of the National Academy of Sciences **114**, E19 (2017).
 - [17] C. N. Kaplan, H. Tu, R. A. Pelcovits, and R. B. Meyer, Physical Review E **82**, 021701 (2010).